

## 3D and 4D printable dual cross-linked polymers with high strength and humidity-triggered reversible actuation

Zhen Jiang, Peidong Shen, Ming Li Tan, Qiao Yan, Jekaterina Viktorova, Chiara Cementon,  
Xiaotong Peng, Pu Xiao and Luke A. Connal\*

Research School of Chemistry, Australian National University

Canberra, ACT 2601 (Australia)

Email: Luke.connal@anu.edu.au

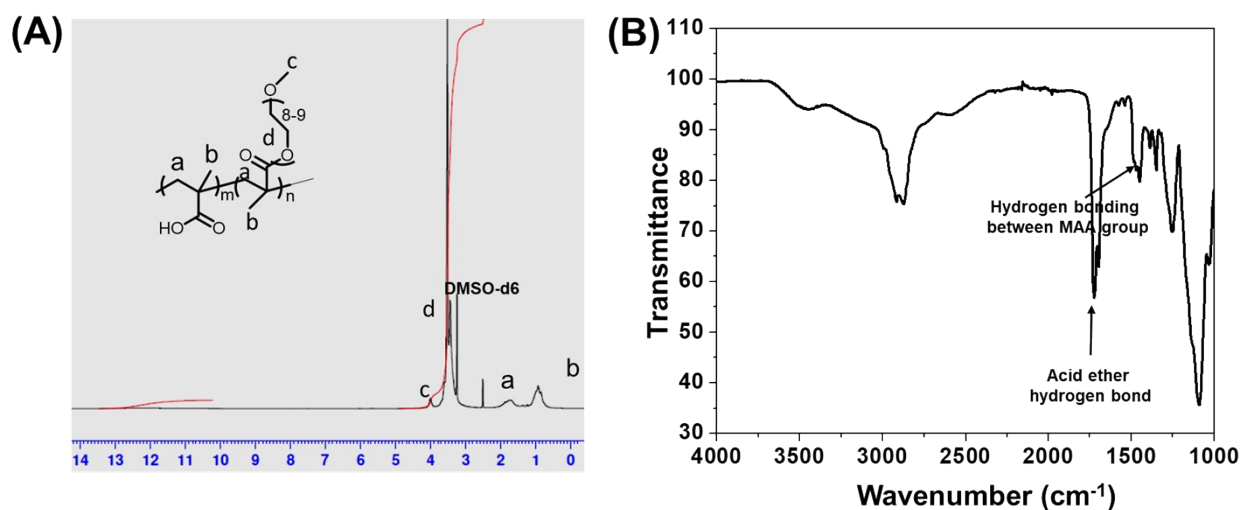
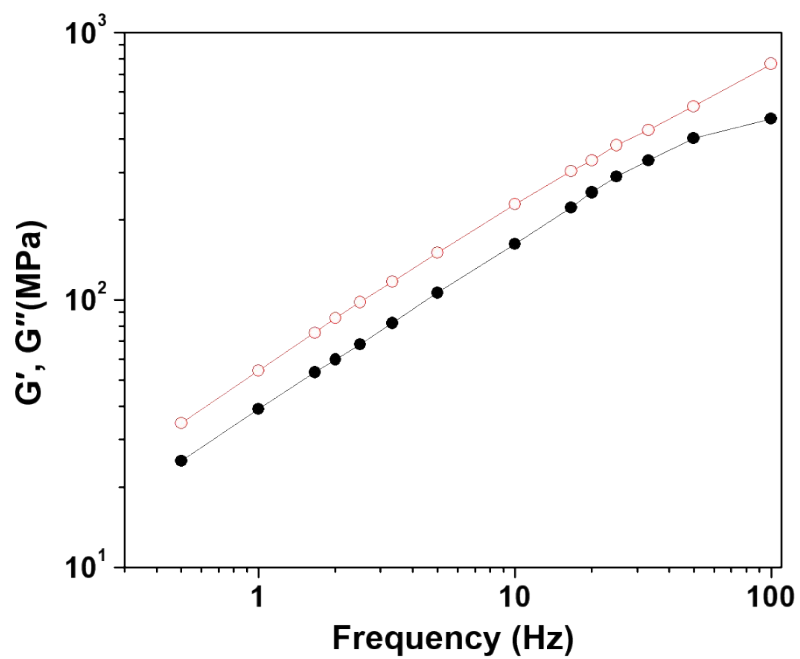
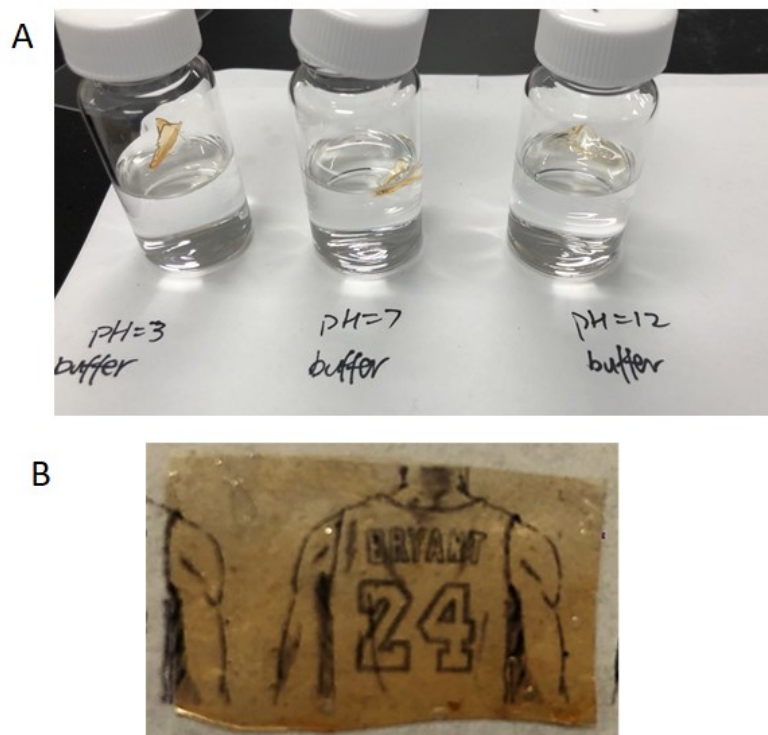


Figure S1. (A) <sup>1</sup>H-NMR and (B) FTIR spectra of poly(MAA-co-OEGMA).



**Figure S2.** Frequency dependency of storage (solid dots,  $G'$ ) and loss (hollow dots,  $G''$ ) moduli of dry H-bonded network poly(MAA-co-OEGMA).



**Figure S3.** **A)** Photography showing the stability of double crosslinked film in aqueous solutions with different pH. **B)** Photographs of the double crosslinked film [with iron(III):COOH molar ratio of 1:75] showing the transparence of the film.

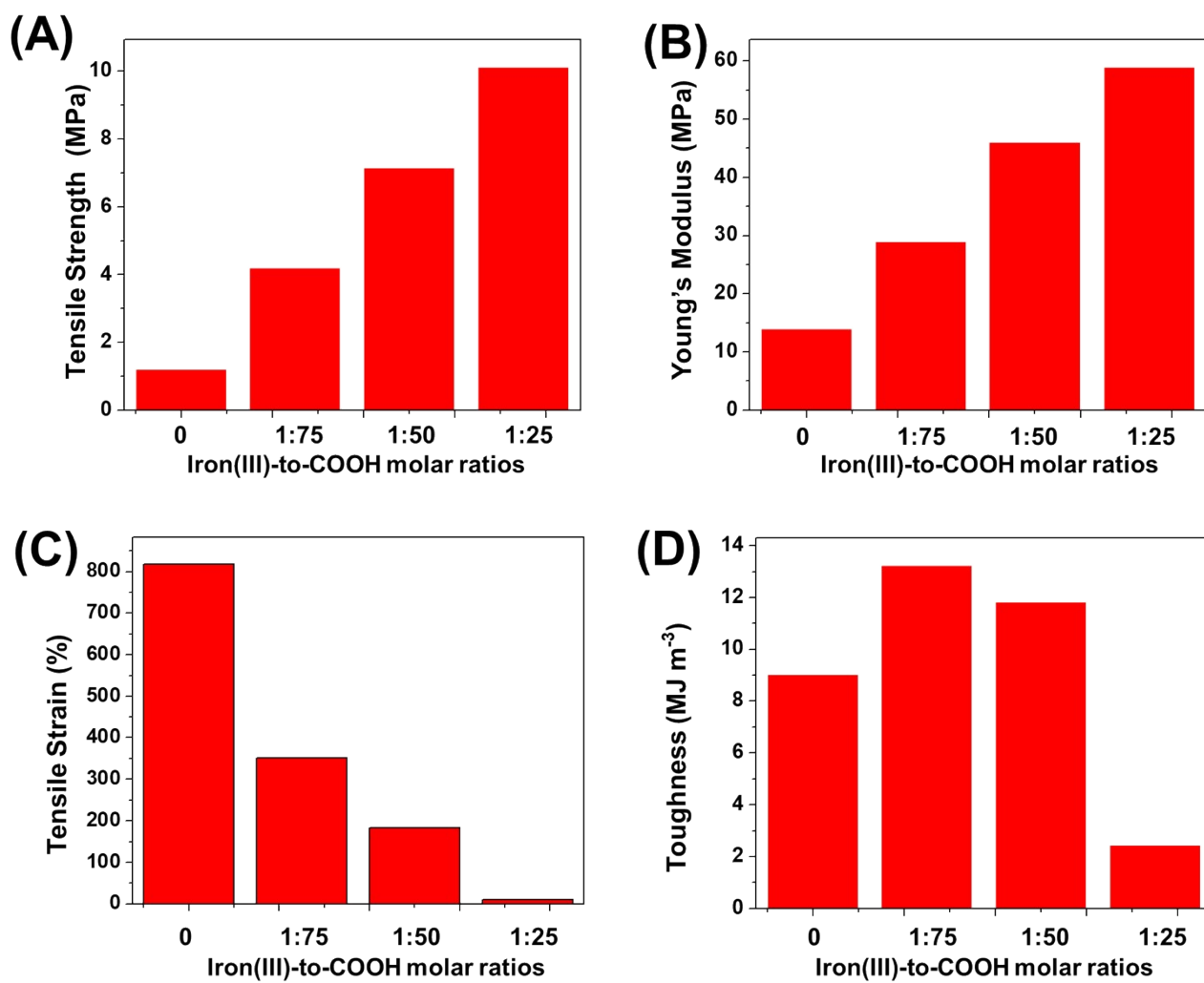


**Figure S4.** Tensile Strength (A), Young's modulus (B), tensile strain (C) and toughness (D)

of the double crosslinked polymers with different iron(III)-to-COOH molar ratios.

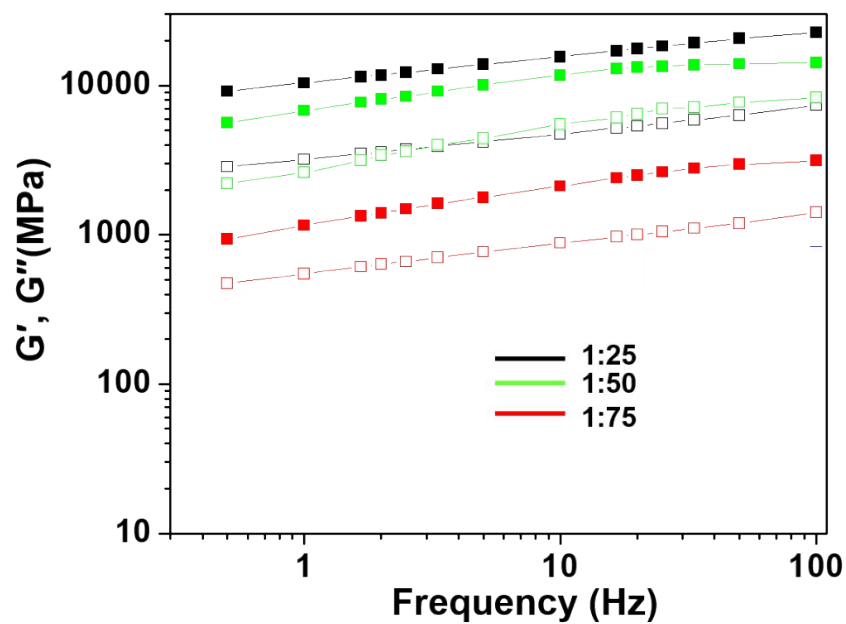


**Figure S5.** Frequency dependency of storage (solid dots,  $G'$ ) and loss (hollow dots,  $G''$ ) moduli of double crosslinked polymers with varying iron(III)-to-COOH molar ratios.

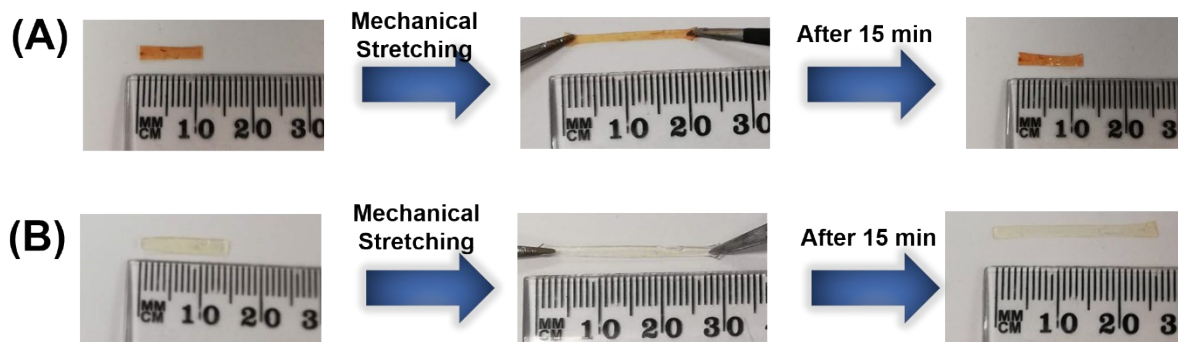


**Figure S6.** Photographs of the double crosslinked (A) and H-bonded (B) network in initial, stretching and unloading status, respectively.

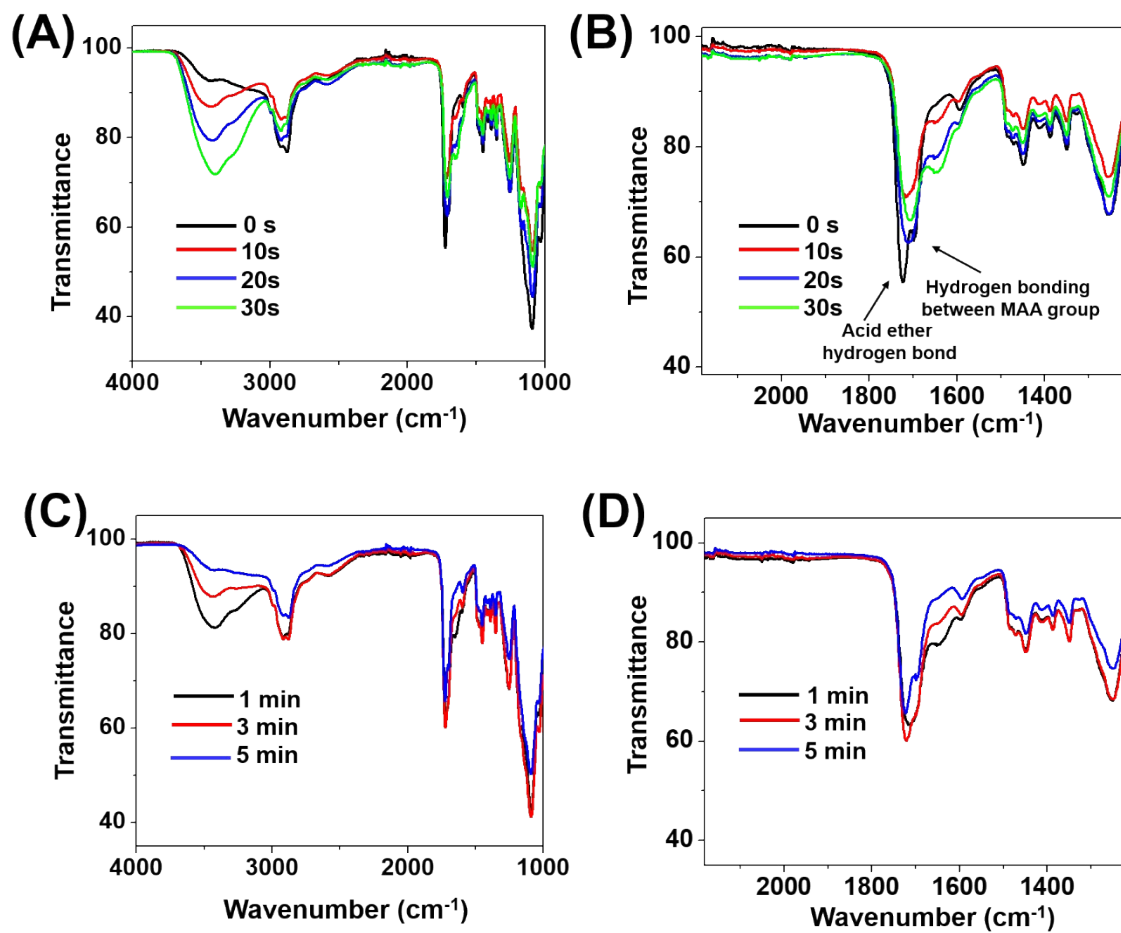


**Figure S7.** FTIR spectra of double crosslinked polymer after absorption of moisture (A, B) in the region of (A, C) 4000-2000 cm<sup>-1</sup> and (B, D) 2100-1200 cm<sup>-1</sup>, and subsequent left in the dry condition (C, D).

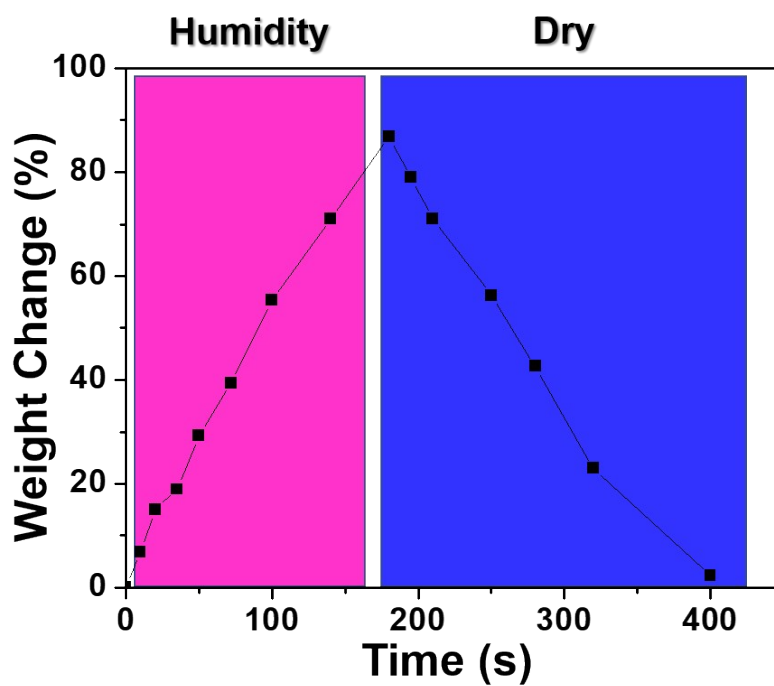


**Figure S8.** The weight change of the double crosslinked polymer during the humidification and dry process.

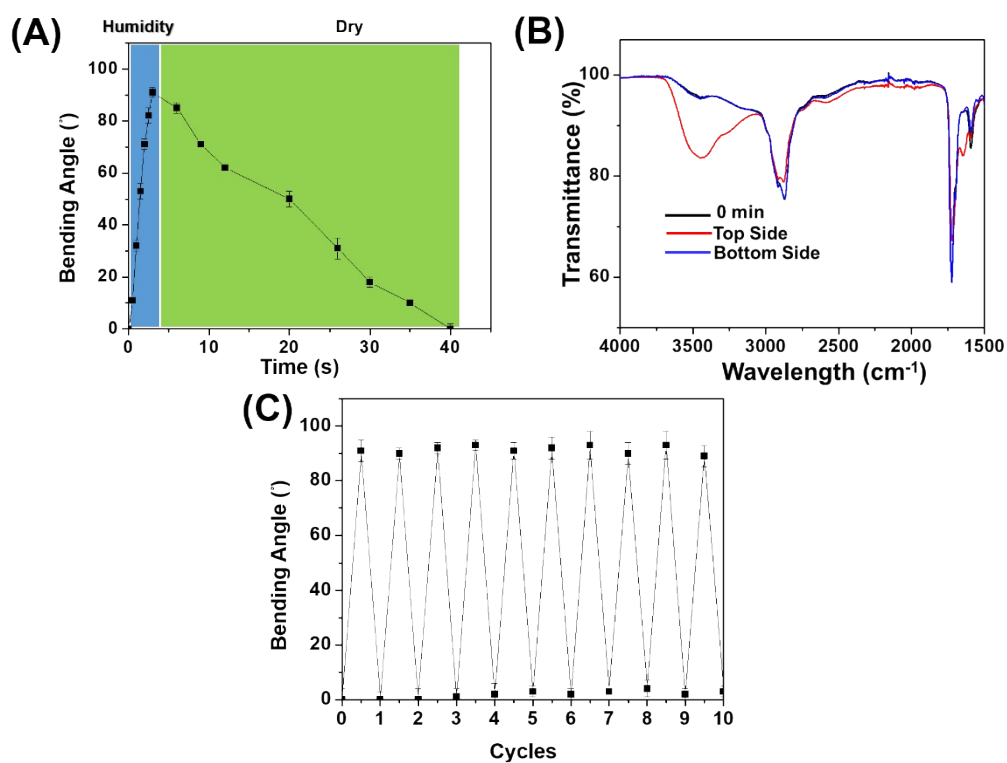


**Figure S9.** (A) Variation of bending angles of the double crosslinked polymer with time upon exposure to humidity and relaxation dynamics after removing the humidity exposure. (B) FTIR spectral for the top and bottom sides of the film under exposure to humidity. (C) Repeatability of the shape transition during the humidification and de-humidification cycles.



**Figure S10.** Time-lapse images of the bending response of the H-bonded network (Thickness =50  $\mu\text{m}$ ) to water vapor flow and remained in the bent state after switching to dry condition for three hours.

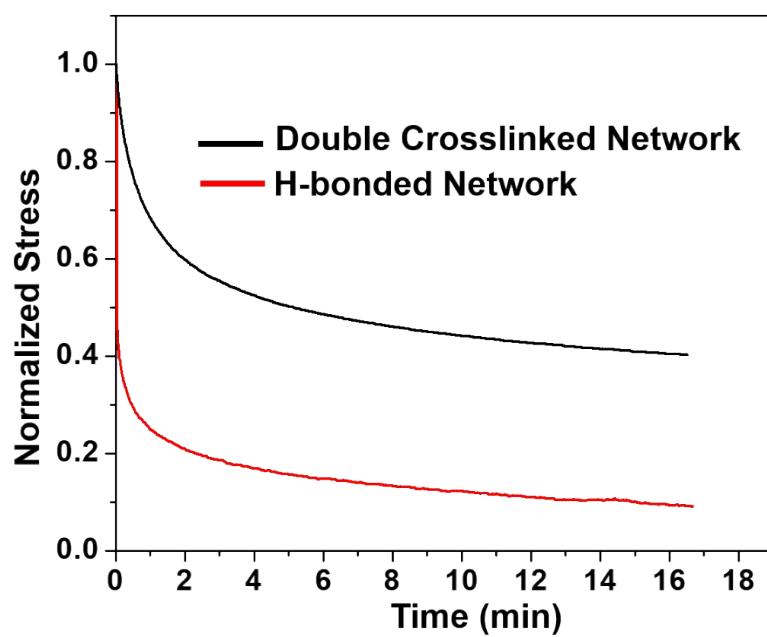


**Figure S11.** Stress relaxation behaviors of wet H-bonded and double crosslinked networks.

Both samples were immersed into the water for 2 min before the tests.

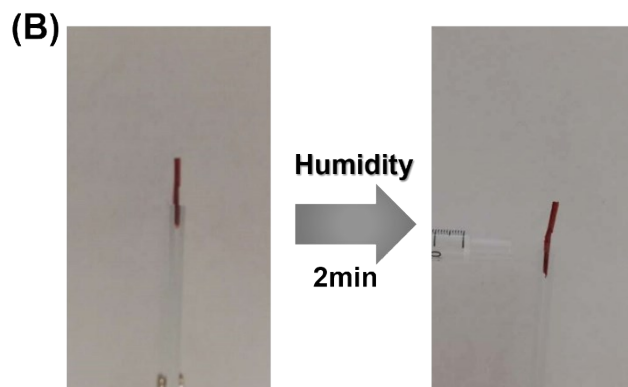
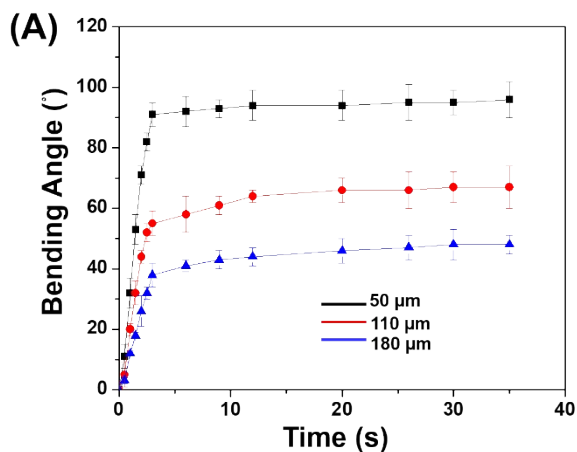


**Figure S12.** (A) Plots showing time dependence of the bending curvature change of double crosslinked polymer films with different thickness upon exposure to humidity. (B) Time-lapse images of the humidity response of the double crosslinked polymer with thickness of 500  $\mu\text{m}$  upon exposure to humidity.

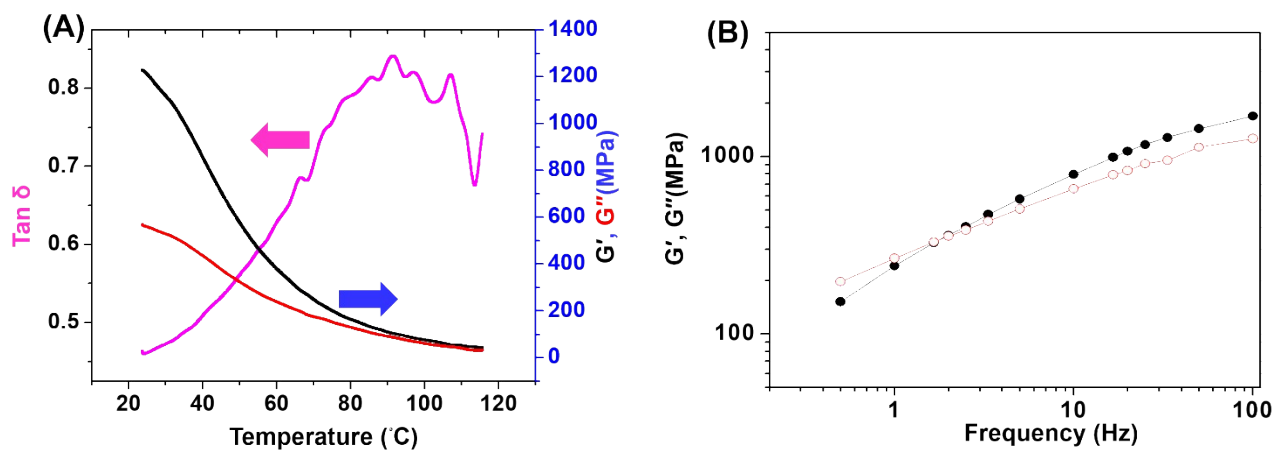


**Figure S13.** (A) Temperature dependence of the storage modulus  $G'$ , loss modulus  $G''$  and the loss factor  $\tan \delta$  of double crosslinked polymer. (B) Frequency dependency of storage (solid dots,  $G'$ ) and loss (hollow dots,  $G''$ ) moduli of wet double crosslinked polymer.

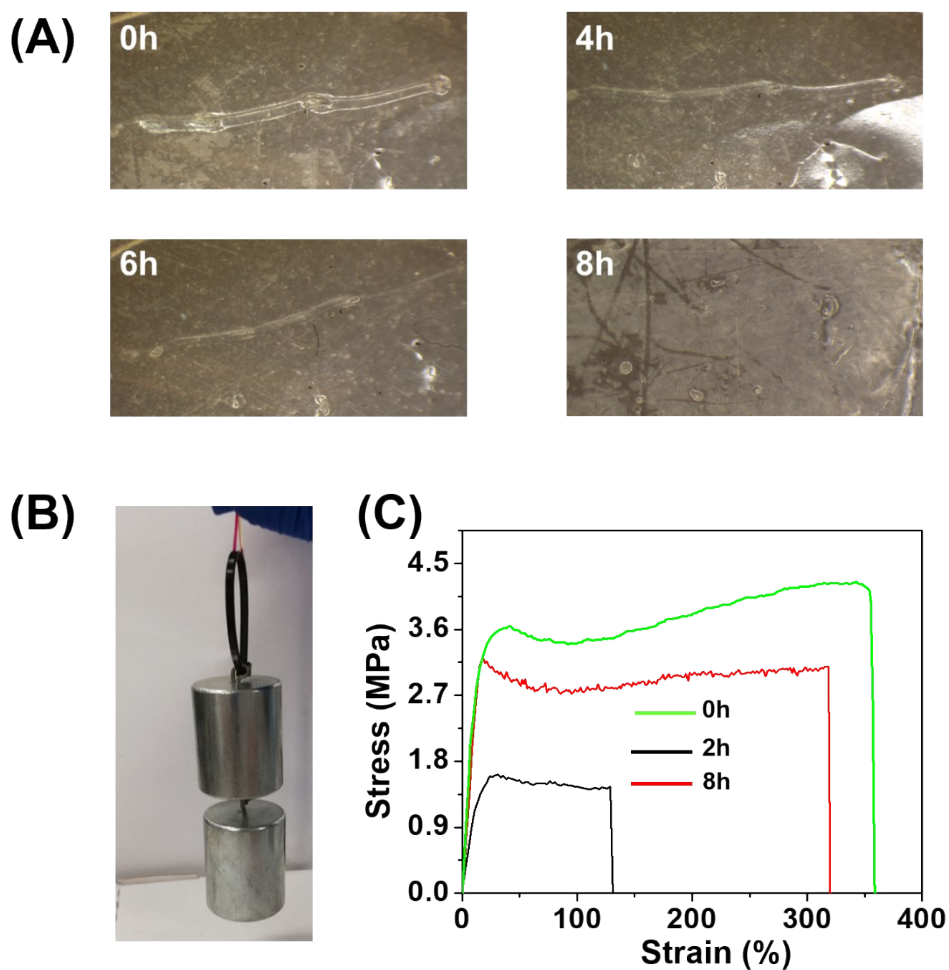
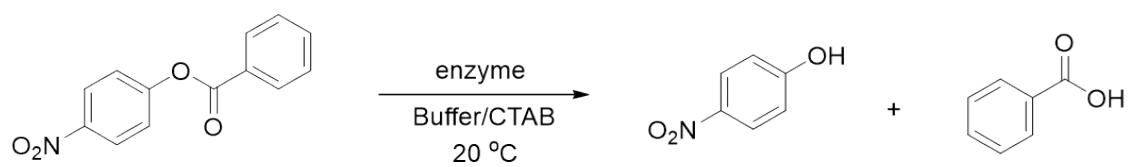


**Figure S14.** (A) Micro-images of the self-healing process of wet double crosslinked polymer under polarizing optical microscopy. (B) Photographs showing qualitative evidence of self-healing; after healing for 8h the polymer can sustain a large strain and held a weight that was 526 times greater than the film weight. (C) Quantitative evidence for self-healing comparing the stress–strain curves for wet double crosslinked polymer at different healing times.



Buffer: Borax/Hydrochloric acid, pH 9.0 (20 °C)

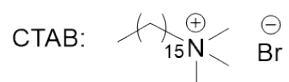


**Figure S15.** Schematic representation of enzyme catalyzed reaction.

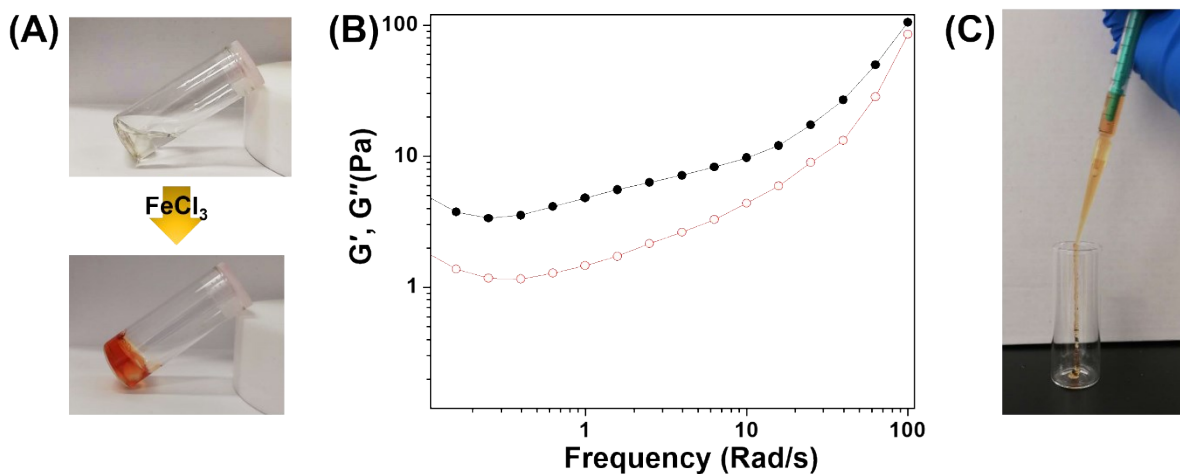


**Figure S16.** (A) Photographs showing the sol-to-gel transition occurs within seconds after adding ferric ions and the gel passes the inversion test. (B) Frequency dependency of storage (solid dots,  $G'$ ) and loss (hollow dots,  $G''$ ) moduli of the hydrogel generated as a result of ferric ions. (C) The steady flow of hydrogel out of the nozzle.

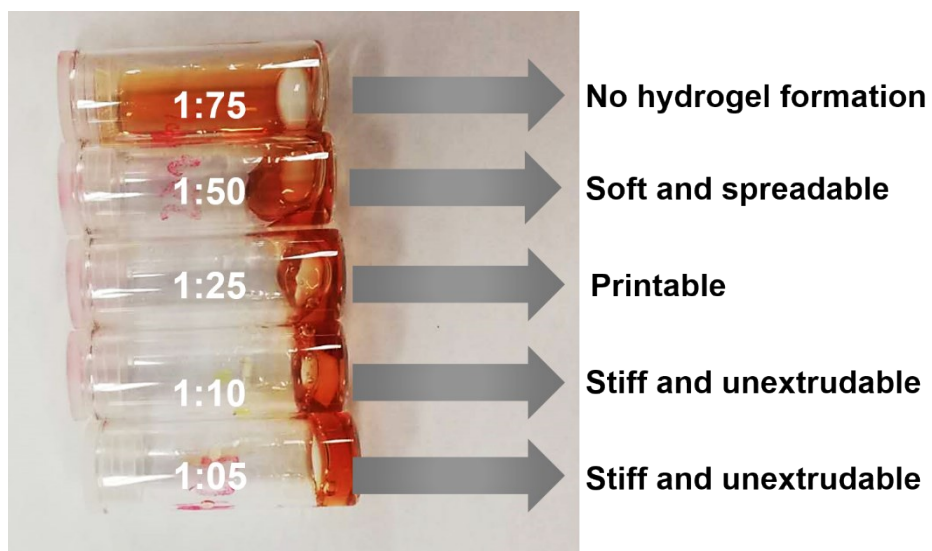


**Figure S17.** Photographs of concentrated aqueous solution of poly(MAA-co-OEGMA) after addition of ferric ions with different iron(III)-to-COOH molar ratios. An optimal formulation for 3D-printing was achieved by using hydrogels with iron(III)-to-COOH molar ratio of 1:25.

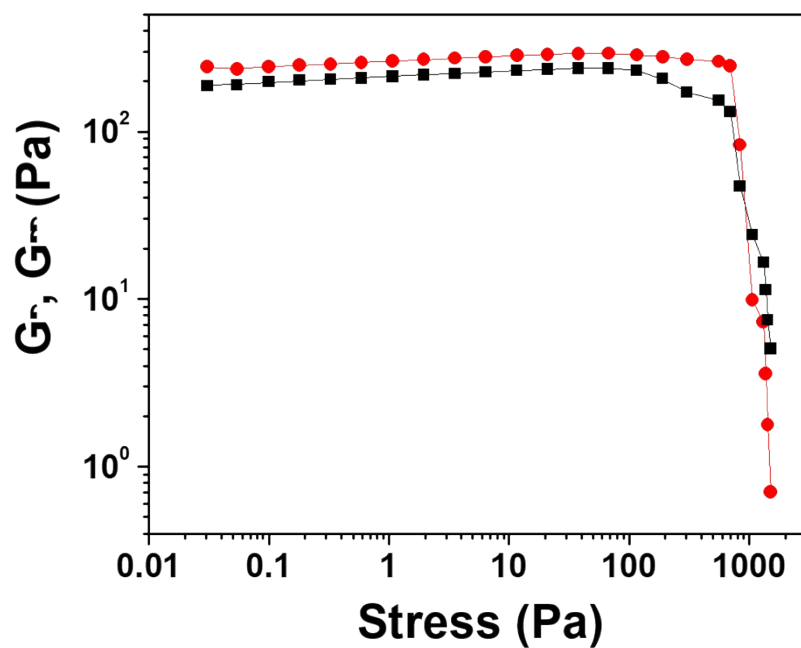


**Figure S18.** Storage (red) and loss modulus (black) of prepared ink (iron(III)-to-COOH molar ratio of 1:25) versus stress showing the corresponding yield stress at 521 Pa.